

An accurate LED-BGK solver on unstructured adaptive meshes (Local Extremum Diminishing interpolation)

Chong A. Kim

Princeton Univ., NJ

Antony Jameson

Princeton Univ., NJ

Luigi Martinelli

Princeton Univ., NJ

Kun Xu

Hong Kong Univ. of Science and Technology, Kowloon

AIAA, Aerospace Sciences Meeting & Exhibit, 35th, Reno, NV, Jan. 6-9, 1997

Starting from the collisional BGK model of the full Boltzmann equation, we develop an accurate and robust finite volume gas kinetic scheme on an unstructured triangular mesh. The numerical approach is composed of two steps: an initial reconstruction step and a gas evolution step. In the initial reconstruction step, the unstructured version of the LED (Local Extremum Diminishing) interpolation is applied to the conservative variables and to compute left and right states along a node edge. In the gas evolution step, the local integral solution of the BGK model is used to compute numerical fluxes at a cell interface. The collisional BGK model provides an alternative to Riemann solvers and possesses many desirable properties that cannot be found in Godunov-type schemes. A classic h-refinement adaptive procedure is implemented to increase the spatial resolution of physically important phenomena such as shock waves, contact discontinuities, or expansion waves with minimal computational costs and memory overheads. It involves mesh enrichment/coarsening steps to either insert nodes on an edge center in high-gradient under-resolved regions or delete nodes in over-resolved regions. Numerical results of several test cases for unsteady compressible inviscid flows are presented. To verify the accuracy and robustness of the current numerical approach, the computed results are compared with the results of structured mesh calculations and other flux splitting methods. (Author)

An Accurate LED-BGK Solver on Unstructured Adaptive Meshes

Chong Am Kim, Antony Jameson† and Luigi Martinelli‡*

Department of Mechanical and Aerospace Engineering, Princeton University
Princeton, New Jersey 08544 U.S.A.

and

Kun Xu§

Department of Mathematics, Hong Kong University of Science and Technology
Clear Water Bay, Kowloon, Hong Kong

Abstract

Starting from the collisional BGK model of the full Boltzmann equation, we develop an accurate and robust finite volume gas kinetic scheme on unstructured triangular mesh. The numerical approach is composed of two steps - an initial reconstruction step and a gas evolution step. In the initial reconstruction step, the unstructured version of the LED (Local Extremum Diminishing) interpolation is applied to the conservative variables and to compute left and right states along a node edge. In the gas evolution step, the local integral solution of BGK model is used to compute numerical fluxes at a cell interface. The collisional BGK model provides an alternative to Riemann solvers and possesses many desirable properties that can not be found in Godunov-type schemes. A classic h -refinement adaptive procedure is implemented to increase the spatial resolution of physically important phenomena such as shock waves, contact discontinuities or expansion waves with minimal computational costs and memory overheads. It involves mesh enrichment/coarsening steps to either insert nodes on an edge center in high-gradient under-resolved regions or delete nodes in over-resolved regions. Numerical results of several test cases for unsteady compressible inviscid flows are presented. To verify the accuracy and robustness of the current numerical approach, the computed results are compared with the results of structured mesh calculations and other flux splitting methods.

* Research Assistant

†James S. McDonnell Distinguished University Professor of Aerospace Engineering, AIAA Fellow

‡Assistant Professor of Aerospace Engineering, AIAA member

§Assistant Professor, AIAA member

Copyright ©1997 by the authors. Published by the American Institute of Aeronautics and Astronautics, Inc. with permission.

1 Introduction

Considerable progress has been made in the areas of compressible flow solvers and solution strategies over the past few decades. At the same time, we have observed tremendous advances in computer storages, speeds and architectures. These two factors have made it possible to compute steady compressible flows over three dimensional realistic body or highly unsteady flows that contain many physical scales. Accurate computations of unsteady compressible flows over complex geometry present a challenge. This is partly due to the complex physical interactions of linear and non-linear waves. As the unsteady computation of complex flows is becoming the essential tool of both practical application and fundamental research, there is a need to design a low-dissipative, robust numerical scheme on unstructured mesh.

A high resolution scheme can be examined in terms of an initial reconstruction and a gas evolution procedure. Higher order (more than second order) interpolation on unstructured mesh is much more involved than that of structured mesh since neighboring cell vertices are not, in general, co-linear. Additionally, all interpolated values should be reduced to first order accuracy to exclude unphysical oscillation across local extrema. Therefore, it seems reasonable to keep second order accuracy in both spatial and time discretization, and introduce a local mesh refinement step to preserve the required accuracy. Recently, Jameson has developed the theory of non-oscillatory positive schemes in terms of the LED criteria ([13]). Flux limited dissipation schemes based on the LED criteria have been implemented and validated for both inviscid and viscous flow computations on structured mesh ([29], [15]). It has been observed that the LED interpolation, unlike the TVD (Total Variation Diminishing) interpolation, can be extended to unstructured mesh with

maintaining the positive coefficients of the discrete form in scalar conservation law. This can be carried out by calculating gradients of appropriate neighboring triangles or edges and applying a monotonic limiter.

Riemann solvers, approximate or exact, have gained much popularity as a way to describe the gas evolution process([9], [27], [12]). In most test cases, Riemann solvers produce good results. After widespread application and intense investigation, however, it has been found that Riemann solvers could produce unphysical solutions such as expansion shocks, carbuncle phenomena or failure of local linearization, etc([8], [24], [15]). Although most of the problems can be cured by adding *ad hoc* techniques, the robustness of original approach seems to be blurred as a result of incomplete fixes. Over the past few years, there has been continuous development of the gas kinetic method based on the collisional BGK model([32], [33], [16], [34]). Previous studies have unveiled interesting properties of BGK-type schemes. Firstly, they satisfy the entropy and the positivity condition which are required to compute wide range of compressible inviscid flows. Secondly, they possess a multi-dimensional gas evolution character and the interpolation in the initial reconstruction step is quite flexible. Thirdly, the BGK model produces the Navier-Stokes equation and describes higher order gas evolution. Those properties, however, can not be found in most popular Riemann solvers and are generally regarded as limitations. Therefore, it is not surprising that BGK-type schemes can overcome many weaknesses of Riemann solvers. This indicates that collisional BGK solvers are good alternatives to Riemann solvers for the gas evolution step.

BGK-type schemes are different from the class of schemes called Boltzmann-type schemes([21], [23]). The physical model for those schemes is the collisionless Boltzmann equation, which does not include the dynamical correlation between left and right moving particles. The missing correlation corresponds to a gas kinetic Lax-Wendroff step and in BGK-type schemes, it is coupled to kinetic flux vector splitting through particle collision time. It has also been pointed out that Boltzmann-type schemes have intrinsically large numerical viscosity and heat conductivity([20]). BGK-type schemes make local use of the full integral solution of the BGK model in the finite volume framework. It is then possible to compute a time-dependent gas distribution function at a cell interface and to obtain the numerical fluxes. This approach provides a physical model for particle collision designed to reduce the large numerical viscosity which is intrinsic in any Boltzmann-type scheme based on the collisionless Boltzmann equation. BGK-type schemes also give Navier-Stokes solutions which follow directly from the BGK model,

and the gas relaxation from an initial nonequilibrium to a final equilibrium state is associated with an increase of entropy.

To increase efficiently the resolution of physically important local phenomena, a mesh adaptation strategy is essential. In this sense, unstructured based flow solver is very desirable due to the inherent flexibility of mesh adaptation. Most popular mesh adaptation strategies can be classified into two approaches: mesh movement(*r*-refinement) and mesh enrichment (*h*-refinement). The *r*-refinement method redistributes existing nodes at every adaptation, clustering them towards positions where the solution gradient is relatively large. An advantage of the *r*-refinement method is that the total number of nodes and the grid topology are conserved. Therefore, there is no computational overhead on a flow solver and the flow solver is amenable to parallelization. However, the possibility of edge crossing during nodes movement or the need for re-meshing make this approach cumbersome. Additionally, an accurate estimate of solution error and conservation of mesh smoothness after adaptation become difficult([3]). On the other hand, the *h*-refinement method alters the number of nodal points by adding or deleting nodes within the computational domain. Since only specific regions of the computational domain are altered, the node density can be locally controlled and the regularity of the initial mesh can be maintained. Another advantage of *h*-refinement method with respect to *r*-refinement method is that the error indicator only needs to be sensitive enough to trigger mesh enrichment when there is a rapid variation of flow field. In the analysis of unsteady flow with adaptation strategy, it is necessary not only to refine high-gradient under-resolved regions but also de-refine over-resolved regions. The adaptation routine therefore consists of mesh enrichment/coarsening steps.

In the present work, an unstructured version of the LED interpolation is implemented in the reconstruction of initial data. An advanced BGK-type scheme which has been designed by the authors is employed to obtain fluxes in the gas evolution step. Then a *h*-refinement adaptation routine is introduced to increase spatial resolution. In section 2, the finite volume LED-BGK scheme is described in terms of the LED interpolation and a BGK flow solver. In section 3, the mesh adaptation strategy adopted is described in detail and the initial mesh generation method is briefly mentioned. Finally, in section 4, numerical results for test cases which contain typical characteristics of high speed unsteady flows are given. These are compared with structured mesh results or other popular flux splitting methods, such as characteristic splitting using Roe's average and CUSP(Convective Upwind Splitting Pressure) splitting.

2 Finite Volume LED-BGK Solver

In gas kinetic theory, it is assumed that the macroscopic fluid flow results from the collective motion of a large number of molecules. The complete description of a particle motion is assumed to be described by the governing equation of the particle distribution function $f(\vec{x}, t, \vec{u}, \xi)$, where \vec{x} is a space variable vector, t is a time variable, \vec{u} is a particle velocity vector in phase space and ξ is the internal degree of freedom. Therefore, the most important step in a finite volume gas kinetic scheme is to construct the time-dependent gas distribution function f at a cell interface. All flow variables or numerical fluxes can be computed by moments of f in phase space. The numerical construction of a distribution function comes from the interpolation of macroscopic flow variables at the cell interface. The interpolation technique can be applied to the conservative, characteristic or primitive variables. In the present work, we applied the LED interpolation to the conservative variables.

2.1 The LED Interpolation

At the beginning of each time step, cell averaged mass, momentum and energy are given. For a higher order scheme, interpolation techniques should be used to capture subcell structure. The most successful interpolation techniques developed so far are usually based on the TVD, ENO and LED principles([10], [11], [28], [13]). Although most of these approaches have been developed mainly for structured mesh, they can be applied to unstructured mesh by extending the one-dimensional concept. A unique feature of the LED interpolation is that the semi-discrete form for scalar conservation law satisfies the positivity condition regardless of mesh types([13]). Let us consider triangles as sketched in Fig.1. Flow variables are defined at cell vertex and control volume is a centroid dual. Let \vec{l}_{oj} be the vector connecting the edge jo and define the neighboring slopes as

$$\Delta^+ v_{jo} = \vec{l}_{jo} \cdot \nabla^+ v, \quad \Delta^- v_{jo} = \vec{l}_{jo} \cdot \nabla^- v,$$

where $\nabla^\pm v$ are the gradients of v evaluated in the neighboring triangles Δopq and Δjrs . Arminjon and Dervieux have used a similar definition([1]). Then the neighboring slopes can be expressed as

$$\begin{aligned} \Delta^+ v_{jo} &= \epsilon_{js}(v_s - v_j) + \epsilon_{jr}(v_r - v_j), \\ \Delta^- v_{jo} &= \epsilon_{op}(v_p - v_o) + \epsilon_{oq}(v_q - v_o), \end{aligned}$$

where the coefficients $\epsilon_{js}, \epsilon_{jr}, \epsilon_{op}, \epsilon_{oq}$ are non-negative, since

$$\epsilon_{js} = \frac{l_{oj}l_{jr}}{2A_{jrs}} \sin(\theta_1), \quad \epsilon_{jr} = \frac{l_{oj}l_{js}}{2A_{jrs}} \sin(\theta_2),$$

$$\epsilon_{op} = \frac{l_{oj}l_{oq}}{2A_{opq}} \sin(\theta_4), \quad \epsilon_{oq} = \frac{l_{oj}l_{op}}{2A_{opq}} \sin(\theta_3).$$

Here, l_{ab} is the length of the edge connecting nodes (a, b) , A_{abc} is the area of the Δabc and θ_i is the angle between an edge and local coordinate (see Fig.1). Therefore, the slopes of appropriate edges give positive contributions to the neighboring slopes. If a neighboring edge is co-linear to the edge jo , the slope of the neighboring edge is chosen as the neighboring slope instead of evaluating gradient. Then the left and right states across the cell interface $s = s_c$ are (see Fig.1)

$$\begin{aligned} v^l &= v_o + 0.5L(\Delta^+ v_{jo}, \Delta^- v_{jo}), \\ v^r &= v_o - 0.5L(\Delta^+ v_{jo}, \Delta^- v_{jo}), \end{aligned}$$

where $L(u, v)$ is a limited average which satisfies the following properties.

- P1. $L(u, v) = L(v, u)$
- P2. $L(\alpha u, \alpha v) = \alpha L(u, v)$
- P3. $L(u, u) = u$
- P4. $L(u, v) = 0$ if u and v has an opposite sign, otherwise $L(u, v)$ has the same sign as u and v .

Standard limiters can be incorporated into L operators. In this paper, α_2 Mean limiter of $L(u, v) = S(u, v) \text{Min}(\frac{|u+v|}{2}, \alpha|u|, \alpha|v|)$ with $\alpha = 2$ is used, where $S(u, v) = \frac{1}{2}(\text{sign}(u) + \text{sign}(v))$.

2.2 A BGK Flow Solver

To avoid mathematical complexity, we present a two-dimensional BGK flow solver. Since a single scalar distribution function f contains all information about the macroscopic flow variables as well as their transport coefficients, the BGK solver in three-dimensions can be derived in a similar way. The BGK model in two-dimensions can be written as

$$f_t + u f_x + v f_y = \frac{g - f}{\tau}, \quad (1)$$

where f is the real gas distribution function and g is the equilibrium state approached by f over a collision time scale τ . Both f and g are functions of space (x, y) , time t , particle velocity (u, v) and internal degree of freedom ξ . The particle collision time τ depends on the local macroscopic flow variables, such as temperature and density. The equilibrium state is usually assumed to be a Maxwellian, with the formulation of

$$g = \rho \left(\frac{\lambda}{\pi}\right)^{\frac{K+2}{2}} e^{-\lambda[(u-U)^2 + (v-V)^2 + \xi^2]},$$

where ρ is the density, (U, V) are the macroscopic velocities in (x, y) directions. When the particle motion in z -direction is included as an internal degree of freedom, the total number of degree of freedom K is equal to $(5 - 3\gamma)/(\gamma - 1) + 1$. The relations

between mass ρ , momentum (P, Q) and energy densities ϵ with the distribution function f are

$$\begin{pmatrix} \rho \\ P \\ Q \\ \epsilon \end{pmatrix} = \int f \psi_\alpha d\Xi, \quad \alpha = 1, 2, 3, 4, \quad (2)$$

where ψ_α is the vector of moments

$$\psi_\alpha = [1, u, v, \frac{(u^2 + v^2 + \xi^2)}{2}]^T,$$

and $d\Xi = dudvd\xi$ is the volume element in phase space. Since mass, momentum and energy are conserved during particle collisions, f and g must satisfy the conservation constraint of

$$\int (g - f) \psi_\alpha d\Xi = 0, \quad \alpha = 1, 2, 3, 4, \quad (3)$$

at all (x, y) and t .

Here, we examine the relation between the BGK model and governing equations of fluid dynamics. In a smooth region, it is reasonable to assume that the flow is in a local thermodynamic equilibrium state. For the equilibrium state with $f = g$, the BGK model becomes the same form as the collisionless Boltzmann equation and the Euler equations can be obtained by taking the moments of ψ_α to Eq.(1). This yields

$$\int (g_t + ug_x + vg_y) \psi_\alpha d\Xi = 0,$$

and the corresponding Euler equations are

$$\begin{pmatrix} \rho \\ \rho U \\ \rho V \\ \frac{\rho}{2}(U^2 + V^2 + \frac{K+2}{2\lambda}) \end{pmatrix}_t + \begin{pmatrix} \rho U \\ \rho U^2 + \frac{\rho}{2\lambda} \\ \rho UV \\ \frac{\rho U}{2}(U^2 + V^2 + \frac{K+4}{2\lambda}) \end{pmatrix}_x + \begin{pmatrix} \rho V \\ \rho UV \\ \rho V^2 + \frac{\rho}{2\lambda} \\ \frac{\rho V}{2}(U^2 + V^2 + \frac{K+4}{2\lambda}) \end{pmatrix}_y = 0,$$

where the pressure term is $p = \rho/2\lambda$.

In a physically dissipative region, the flow is in a non-equilibrium state. The behavior of f in this region can be quantitatively examined by the Chapman-Enskog expansion([17]). Up to the first order of τ , the departure of f from an equilibrium state is $f = g - \tau(g_t + ug_x + vg_y)$. Taking moments of ψ_α to Eq.(1) with this f , we get

$$\begin{aligned} & \int (g_t + ug_x + vg_y) \psi_\alpha d\Xi = \\ & \tau \int (g_{tt} + 2ug_{xt} + 2vg_{yt} + 2uv g_{xy} + u^2 g_{xx} + v^2 g_{yy}) \psi_\alpha d\Xi. \end{aligned}$$

After integrating out all the moments, the Navier-Stokes equations are obtained as

$$\begin{aligned} & \begin{pmatrix} \rho \\ \rho U \\ \rho V \\ \frac{\rho}{2}(U^2 + V^2 + \frac{K+2}{2\lambda}) \end{pmatrix}_t + \begin{pmatrix} \rho U \\ \rho U^2 + \frac{\rho}{2\lambda} \\ \rho UV \\ \frac{\rho U}{2}(U^2 + V^2 + \frac{K+4}{2\lambda}) \end{pmatrix}_x \\ & + \begin{pmatrix} \rho V \\ \rho UV \\ \rho V^2 + \frac{\rho}{2\lambda} \\ \frac{\rho V}{2}(U^2 + V^2 + \frac{K+4}{2\lambda}) \end{pmatrix}_y = \\ & \tau \begin{pmatrix} C_1((K+1)U_x - V_y) \\ C_2(U_y + V_x) \\ C_1 U((K+1)U_x - V_y) + C_2 V(U_y + V_x) + C_3(\frac{1}{\lambda})_x \\ 0 \end{pmatrix}_x + \\ & \tau \begin{pmatrix} C_2(U_y + V_x) \\ C_1((K+1)V_y - U_x) \\ C_2 U(U_y + V_x) + C_1 V((K+1)V_y - U_x) + C_3(\frac{1}{\lambda})_y \\ 0 \end{pmatrix}_y, \quad (4) \end{aligned}$$

where $C_1 = \frac{\rho}{(K+2)\lambda}$, $C_2 = \frac{\rho}{2\lambda}$ and $C_3 = \frac{(K+4)\rho}{8\lambda}$. The viscosity coefficient $\mu = \tau p$, the heat conductivity coefficient $\kappa = \mu c_p$ and c_p is a specific heat constant.

After introducing a local coordinate in terms of s (see Fig.1), the general solution of f at the cell interface $s = s_c$ and time t is

$$f(s_c, t, u, v, \xi) = \frac{1}{\tau} \int_0^t g(s', t', u, v, \xi) e^{-(t-t')/\tau} dt' + e^{-t/\tau} f_0(s_c - ut - vt), \quad (5)$$

where $s' = s_c - u(t-t') - v(t-t')$ is the trajectory of a particle motion and f_0 is the initial non-equilibrium distribution function f at the beginning of each time step. From Eq.(5), we may notice that g and f_0 must be specified in order to obtain f .

Generally, f_0 and g around the cell interface are assumed to be

$$f_0 = \begin{cases} g^l (1 + a^l(s - s_c)), & s \leq s_c \\ g^r (1 + a^r(s - s_c)), & s \geq s_c \end{cases} \quad (6)$$

and

$$g = g_0 [1 + (1 - H[s - s_c]) \bar{a}^l (s - s_c) + H[s - s_c] \bar{a}^r (s - s_c) + \bar{A} t], \quad (7)$$

where g^l, g^r and g_0 are local Maxwellian distribution functions to be determined, which are located, respectively, to the left, to the right and in the middle of a cell interface. $a^l, a^r, \bar{a}^l, \bar{a}^r, \bar{A}$ are local spatial and time slopes and $H[s]$ is the unit step function. In the expansion of g , the possibility of discontinuous slopes has been allowed. This increases substantially the robustness of the present scheme without sacrificing accuracy. The dependence of slopes ($m = a, \bar{a}, \bar{A}$) on the particle velocities can be

obtained from the Taylor expansion of a Maxwellian and has the form

$$m^* = m_1^* + m_2^* u + m_3^* v + m_4^* \frac{(u^2 + v^2 + \xi^2)}{2} = m_\alpha^* \psi_\alpha,$$

where all coefficients of $m_1^*, m_2^*, m_3^*, m_4^*$ are local constants and * stands for the left(l) or right(r) state. The idea of interpolating f_0 separately across the cell interface originates from the following physical consideration: for a gas flow in a physically dissipative region, since the cell size is typically much larger than the thickness of a discontinuity, the physical quantities can change dramatically in space. For example, across a shock front, the upstream and downstream gas distribution functions could be two different Maxwellians. Therefore, we need a splitting of f_0 to capture this physical situation.

In the LED interpolation described in Section(2.1), we have obtained the left and right side pointwise values of $(\rho^l, P^l, \dots, Q^r, \epsilon^r)$. By the relation between the gas distribution function f_0 and the macroscopic variables (Eq.(2)), we get

$$\int g^l \psi_\alpha d\Xi = \begin{pmatrix} \rho^l \\ P^l \\ Q^l \\ \epsilon^l \end{pmatrix}; \quad \int g^l a^l \psi_\alpha d\Xi = \begin{pmatrix} \frac{\rho_j - \rho_o}{\Delta s^-} \\ \frac{P_j - P_o}{\Delta s^-} \\ \frac{Q_j - Q_o}{\Delta s^-} \\ \frac{\epsilon_j - \epsilon_o}{\Delta s^-} \end{pmatrix}$$

and

$$\int g^r \psi_\alpha d\Xi = \begin{pmatrix} \rho^r \\ P^r \\ Q^r \\ \epsilon^r \end{pmatrix}; \quad \int g^r a^r \psi_\alpha d\Xi = \begin{pmatrix} \frac{\rho_j - \rho^r}{\Delta s^+} \\ \frac{P_j - P^r}{\Delta s^+} \\ \frac{Q_j - Q^r}{\Delta s^+} \\ \frac{\epsilon_j - \epsilon^r}{\Delta s^+} \end{pmatrix}, \quad (8)$$

where $\Delta s^- = s_c - s_o$ and $\Delta s^+ = s_j - s_c$ (see Fig.1). With the definition of the Maxwellian distributions for the left and right states

$$g^* = \rho^* \left(\frac{\lambda^*}{\pi} \right)^{\frac{K+2}{2}} e^{-\lambda^* [(u-U^*)^2 + (v-V^*)^2 + \xi^2]},$$

and from Eq.(8), all the parameters in g^* can be uniquely determined from

$$\begin{pmatrix} \rho^* \\ U^* \\ V^* \\ \lambda^* \end{pmatrix} = \begin{pmatrix} \rho^* \\ P^*/\rho^* \\ Q^*/\rho^* \\ \frac{0.25(K+2)\rho^*}{(\epsilon^* - \frac{P^{*2} + Q^{*2}}{2\rho^*})} \end{pmatrix}.$$

Once g^* is obtained from the above equations, the slope of a^* can be computed. For example, for the right state, we get

$$\begin{pmatrix} \frac{\rho_j - \rho^r}{\rho^r \Delta s^+} \\ \frac{P_j - P^r}{\rho^r \Delta s^+} \\ \frac{Q_j - Q^r}{\rho^r \Delta s^+} \\ \frac{\epsilon_j - \epsilon^r}{\rho^r \Delta s^+} \end{pmatrix} \equiv \begin{pmatrix} \Delta \rho^r \\ \Delta P^r \\ \Delta Q^r \\ \Delta \epsilon^r \end{pmatrix} = M_{\alpha\beta}^r \begin{pmatrix} a_1^r \\ a_2^r \\ a_3^r \\ a_4^r \end{pmatrix} = M_{\alpha\beta}^r a_{\beta}^r, \quad (9)$$

where the matrix $M_{\alpha\beta}^r = \frac{1}{\rho^r} \int g^r \psi_\alpha \psi_\beta d\Xi$ is

$$M_{\alpha\beta}^r = \begin{pmatrix} 1 & U^r & V^r & B_1 \\ U^r & U^{r2} + \frac{1}{2\lambda^r} & U^r V^r & B_2 \\ V^r & U^r V^r & V^{r2} + \frac{1}{2\lambda^r} & B_3 \\ B_1 & B_2 & B_3 & B_4 \end{pmatrix},$$

where

$$\begin{aligned} B_1 &= \frac{1}{2}(U^{r2} + V^{r2} + \frac{K+2}{2\lambda^r}), \\ B_2 &= \frac{1}{2}(U^{r3} + V^{r2}U^r + \frac{(K+4)U^r}{2\lambda^r}), \\ B_3 &= \frac{1}{2}(V^{r3} + U^{r2}V^r + \frac{(K+4)V^r}{2\lambda^r}), \\ B_4 &= \frac{1}{4}[(U^{r2} + V^{r2})^2 + \frac{(K+4)(U^{r2} + V^{r2})}{\lambda^r} \\ &\quad + \frac{(K^2 + 6K + 8)}{4\lambda^{r2}}]. \end{aligned}$$

From Eq.(9), $(a_1^r, a_2^r, a_3^r, a_4^r)^T$ can be efficiently obtained by observing that $M_{\alpha\beta}^r$ is a symmetric matrix. Since the matrix $M_{\alpha\beta}^l = \frac{1}{\rho^l} \int g^l \psi_\alpha \psi_\beta d\Xi$ has the same structure of $M_{\alpha\beta}^r$, $(a_1^l, a_2^l, a_3^l, a_4^l)^T$ can be obtained using a similar procedure.

By determining f_0 , the corresponding values of ρ_0, U_0, V_0 and λ_0 in g_0 with

$$g_0 = \rho_0 \left(\frac{\lambda_0}{\pi} \right)^{\frac{K+2}{2}} e^{-\lambda_0 [(u-U_0)^2 + (v-V_0)^2 + \xi^2]}$$

can be determined as follows. Taking the limit $t \rightarrow 0$ in Eq.(5) and substituting its solution into Eq.(3), the conservation constraint at $(s = s_c, t = 0)$ gives

$$\int g_0 \psi_\alpha d\Xi = \int_{u>0} \int g^l \psi_\alpha d\Xi + \int_{u<0} \int g^r \psi_\alpha d\Xi, \quad \alpha = 1, 2, 3, 4. \quad (10)$$

Since λ_0 can be found from ρ_0, U_0, V_0 and ϵ_0 through the relation

$$\lambda_0 = 0.25(K+2)\rho_0 / [\epsilon_0 - \frac{\rho_0(U_0^2 + V_0^2)}{2}],$$

we only need to know $(\rho_0, U_0, V_0, \epsilon_0)^T$, which can be expressed as moments of g^l and g^r . After introducing the notation

$$\langle q \rangle^+ = \frac{1}{\rho^l} \int_{u>0} q g^l d\Xi, \quad \langle q \rangle^- = \frac{1}{\rho^r} \int_{u<0} q g^r d\Xi,$$

from Eq.(10), we obtain

$$\begin{pmatrix} \rho_0 \\ P_0 \\ Q_0 \\ \epsilon_0 \end{pmatrix} = \begin{pmatrix} \rho^l \langle 1 \rangle^+ + \rho^r \langle 1 \rangle^- \\ \rho^l \langle u \rangle^+ + \rho^r \langle u \rangle^- \\ \rho^l \langle v \rangle^+ + \rho^r \langle v \rangle^- \\ \frac{\rho^l}{2} \langle \bar{v}^2 \rangle^+ + \frac{\rho^r}{2} \langle \bar{v}^2 \rangle^- \end{pmatrix}, \quad (11)$$

where $\bar{v}^2 = u^2 + v^2 + \xi^2$. A detailed derivation on the moments $\langle q \rangle^+$ and $\langle q \rangle^-$ can be found in [34],

[16]. Then \bar{a}^l and \bar{a}^r of g in Eq.(7) can be obtained through the relation of

$$\begin{pmatrix} \frac{\rho_j - \rho_0}{\rho_0 \Delta s^+} \\ \frac{P_j - P_0}{\rho_0 \Delta s^+} \\ \frac{Q_j - Q_0}{\rho_0 \Delta s^+} \\ \frac{\epsilon_j - \epsilon_0}{\rho_0 \Delta s^+} \end{pmatrix} = \bar{M}_{\alpha\beta}^0 \begin{pmatrix} \bar{a}_1^r \\ \bar{a}_2^r \\ \bar{a}_3^r \\ \bar{a}_4^r \end{pmatrix} = \bar{M}_{\alpha\beta}^0 \bar{a}_{\beta}^r,$$

and

$$\begin{pmatrix} \frac{\rho_0 - \rho_0}{\rho_0 \Delta s^-} \\ \frac{P_0 - P_0}{\rho_0 \Delta s^-} \\ \frac{Q_0 - Q_0}{\rho_0 \Delta s^-} \\ \frac{\epsilon_0 - \epsilon_0}{\rho_0 \Delta s^-} \end{pmatrix} = \bar{M}_{\alpha\beta}^0 \begin{pmatrix} \bar{a}_1^l \\ \bar{a}_2^l \\ \bar{a}_3^l \\ \bar{a}_4^l \end{pmatrix} = \bar{M}_{\alpha\beta}^0 \bar{a}_{\beta}^l.$$

The matrix $\bar{M}_{\alpha\beta}^0 = \frac{1}{\rho_0} \int g_0 \psi_{\alpha} \psi_{\beta} d\Xi$ has the same structure of $M_{\alpha\beta}^r$. Therefore, $(\bar{a}_1^r, \bar{a}_2^r, \bar{a}_3^r, \bar{a}_4^r)^T$ and $(\bar{a}_1^l, \bar{a}_2^l, \bar{a}_3^l, \bar{a}_4^l)^T$ can be found by following the procedure in Eq.(9).

Up to this point, we have determined two half-Maxwellians(g^l, g^r) for f_0 and one whole Maxwellian distribution function(g_0) at the cell interface and they represent the nonequilibrium state f_0 and equilibrium state g_0 . All the slopes in the expression of a^l, a^r in f_0 and \bar{a}^l, \bar{a}^r in g are obtained from the slopes of macroscopic variables. The construction of two slopes for g gives more freedom to describe complicated flow situations and for Navier-Stokes solutions, the slopes of \bar{a}^l and \bar{a}^r represent the viscosity and heat conduction effects.

After substituting Eq.(6) and Eq.(7) into Eq.(5), the final gas distribution function at a cell interface is expressed as

$$\begin{aligned} f(s_c, t, u, v, \xi) &= (1 - e^{-t/\tau})g_0 + [\tau(-1 + e^{-t/\tau}) \\ &+ te^{-t/\tau}](\bar{a}^l H[u] + \bar{a}^r(1 - H[u]))ug_0 \\ &+ \tau(t/\tau - 1 + e^{-t/\tau})\bar{A}g_0 + e^{-t/\tau}[(1 - uta^l)H[u]g^l \\ &+ (1 - uta^r)(1 - H[u])g^r]. \end{aligned} \quad (12)$$

The only unknown term in Eq.(12) is the time evolution term \bar{A} . Since both f (Eq.(12)) and g (Eq.(7)) contain \bar{A} , we apply again the conservation constraint of Eq.(3) at $s = s_c$ and integrate it over the time step T to get

$$\int_0^T \int (g - f) \psi_{\alpha} d\Xi dt = 0,$$

which gives

$$\begin{aligned} \bar{M}_{\alpha\beta}^0 \bar{A}_{\beta} &= \frac{1}{\rho_0} \int [\gamma_1 u(\bar{a}^l H[u] + \bar{a}^r(1 - H[u])g_0) \\ &+ \gamma_2 u(a^l H[u]g^l + a^r(1 - H[u])g^r)] \psi_{\alpha} d\Xi, \end{aligned} \quad (13)$$

where

$$\begin{aligned} \gamma_0 &= T - \tau(1 - e^{-T/\tau}), \\ \gamma_1 &= (-T + 2\tau(1 - e^{-T/\tau}) - Te^{-T/\tau})/\gamma_0, \\ \gamma_2 &= (Te^{-T/\tau} - \tau(1 - e^{-T/\tau}))/\gamma_0. \end{aligned}$$

All moments of the Maxwellian on the right hand side of Eq.(13) can be found in [34] and the above equation can be solved for $(\bar{A}_1, \bar{A}_2, \bar{A}_3, \bar{A}_4)^T$ as in Eq.(9).

Finally, the numerical fluxes at the cell interface can be computed as

$$\begin{pmatrix} \mathcal{F}_{\rho} \\ \mathcal{F}_P \\ \mathcal{F}_Q \\ \mathcal{F}_{\epsilon} \end{pmatrix}_{s=s_c} = \int_0^T \int u f(s_c, t, u, v, \xi) \psi_{\alpha} d\Xi dt, \quad (14)$$

where $f_{s_c} = f(s_c, t, u, v, \xi)$ is given in Eq.(12).

3 Adaptation Strategy

Any mesh adaptation scheme involves two essential steps : selection of adaptation criteria and a mesh refinement routine. Adaptation criteria detect appropriate regions which need further resolution. An optimal adaptation criterion would provide the error of the computed solution. Since this needs the information on the exact solution, approximate feature detections or error estimate techniques are commonly used. For example, Löhner *et al.* have successfully used an approximate L_2 -norm error([18], [19]). Berger *et al.* have developed an error estimate based on the Richardson extrapolation on rectangular mesh([5], [6]). Although a rigorous analysis on a *posterior* error for a scalar hyperbolic equation has been carried out by Hansboro and Johnson in the context of finite element methods([14]), an estimator in most cases is based on a feature detection technique. In this sense, an error indicator would be a more appropriate terminology than an error estimator. In this paper, a simple feature detection technique has been used to capture regions which need extra flowfield resolution - around a shock wave, a contact discontinuity and expansion waves. For a given triangle, the maximum, minimum and arithmetic average of a flow variable(q) is calculated. Then the approximate magnitude of a flow gradient is measured by

$$\Delta_q = \text{Max}(|\frac{\bar{q} - q_{max}}{\bar{q}}|, |\frac{\bar{q} - q_{min}}{\bar{q}}|),$$

where $q_{max} = \max_i(q_i)$, $q_{min} = \min_i(q_i)$, $\bar{q} = \sum_{i=1}^N q_i/N$. That is, the difference between extrema and the average is normalized by the average value. In practice, if $\Delta_q > \epsilon_q$ for a threshold value ϵ_q , the triangle is flagged for adaptation.

Since the mesh refinement routine is based on the solution obtained by an initial mesh, the initial mesh should be generated to maximize mesh quality. For example, if the initial mesh is too coarse or irregular, the computed results would be unable to resolve or detect certain phenomena giving too poor solutions to be adapted. The initial mesh generation method

adopted in this paper is based on the Rebay's point placement algorithm combined with the Delaunay triangulation([26]). Starting from the given boundary points, the initial triangulation is carried out using the Delaunay criteria. Since the initial mesh is usually unacceptable in term of regularity, an additional point is introduced successively in a position which can produce a regular mesh as a result of the Delaunay triangulation. This routine is iterated until all triangles generated satisfy certain regularity requirement. This method produces a guaranteed high quality mesh for arbitrary two-dimensional geometry and the point placement routine is automatic and robust([2]).

Based on the solution obtained by the initial mesh, the triangles to be adapted are determined according to adaptation criteria. The adaptation level which indicates the degree of adaptation is initialized as zero for all triangles. Adapted triangles are typically divided into four sub-triangles by inserting nodes on edge center and the adaptation level is increased by one. The neighboring triangles which share an edge with adapted triangles are flagged as boundary triangles. They are divided into two sub-triangles and the corresponding adaptation level is increased by half. If a boundary triangle shares more than two edges with adapted triangles, it is also flagged to be adapted. As the level of adaptation increases, however, several other cases are possible(see Fig.2). This method seems to be the most simple way to maintain the regularity and smoothness of the original mesh after mesh enrichment. In fact, similar procedures have been applied successfully to problems involving complex geometry in two or three-dimensions([4], [25], [7]).

In the mesh coarsening step, every triangle which is not flagged in the mesh enrichment step is treated as a candidate for deletion. For each node of a candidate, the adaptation level of neighboring triangles which share the common node is checked. If they are same, the common node is flagged for deletion. If any of the candidates has a different adaptation level, the common node is rejected for deletion. After finishing this process, if the number of nodes for deletion are greater than one, the triangle is coarsened. The adaptation level decreases by one if the triangle is fully coarsened and by half in case of half coarsening(see Fig.2). In this step, the hierarchical tree data structure that has been setup in the previous adaptation is used to check "mother" and "child" triangles. The mesh coarsening step is not necessarily the reverse process of the mesh enrichment step. If a triangle is not coarsened to its mother triangle, the corresponding data structure would change accordingly.

4 Numerical Results

Four standard test cases have been chosen to examine the accuracy and robustness of the current numerical approach. For each case, the adaptation routine is called every four iteration and the maximum level of adaptation is two. Therefore, one initial triangle can be divided into 16 sub-triangles. The CFL number is set to 0.75. In unsteady flow computations, most phenomena to be adapted are transient. To keep track of those accurately during the time intergration, two outer layers are added to adapted regions. For a flow variable to detect a shock wave or expansion fan, pressure is used. To capture contact discontinuity, density or entropy is used. The threshold value for pressure and density is 0.1 and 0.015 for entropy. The computed results are compared with other LED schemes which is based on the characteristic splitting using Roe average(LED-Csplit) and CUSP splitting(LED-CUSP)([13],[15]).

The first test case treats a moving shock with the speed of $M_s = 1.5$ that is propagated in two-dimensional duct of $(x,y) = (1.2,0.2)$. Although this is a relatively simple test, it provides a good way to check shock capturing properties of LED schemes augmented with mesh adaptation. Fig.3 shows density profile along $y = 0.1$ line at five different times. All schemes yield monotonic shock profiles and show an excellent agreement with exact solutions. As we can see from Fig.4, the number of nodes remains almost uniform during the entire adaptation process.

The second test case is the forward facing step with Mach number of 3. Since this test shows many important phenomena which typically happen in unsteady supersonic flows, it has been widely computed, especially on structured mesh([31]). To resolve the behavior of the expansion fan around the step corner, no special treatment such as an entropy fix was required. Fig.5 shows a typical initial mesh distribution. We can see the mesh regularity including the boundary region. The initial mesh contained 4836 nodes. Fig.6 shows the comparison of density distribution at $t = 4$. The results on unstructured mesh without adaptation gives very competitive results with structured mesh calculation. There are 16140 cells in structured mesh and 18110 nodes in unstructured mesh, respectively. Fig.7 shows the effect of adaptation at $t = 3$. Starting from the coarser mesh(4836 nodes), the final adapted mesh(LED-Csplit : 16961, LED-CUSP : 16016, LED-BGK : 17649 nodes) is nicely clustered around shock waves, a contact discontinuity and expansion regions. The corresponding computed results resolve local phenomena very clearly while keeping monotonic profiles. Especially, we can see more clearly the inviscid instability, so called Kelvin - Helmholtz instability, of the contact discontinuity emerging from

the shock triple point in the result of LED-BGK scheme. In the case of LED-Csplitted scheme, the contact discontinuity is relatively diffused and a significant Mach step has been observed. The reason is that if we use the same α_2 Mean limiter as in other LED schemes, the adapted mesh around the step corner produces an over-expansion leading to negative density and/or pressure. A relatively diffusive limiter such as the Minmod limiter had to be used to prevent that. This indicates the importance of robustness in designing a numerical scheme.

The third test case is the double Mach reflection with a shock speed of $M_s = 10.0$. Initially a shock wave with $M_s = 10.0$ is located at the entrance of a 30 degree wedge and propagated along the wedge. The computational domain is a rectangle of length $(x,y) = (4,1)$ and the entrance of the wedge is located at $(x,y) = (1/6,0)$. The initial mesh for this case contained 16986 nodes and the final adapted mesh 36245 nodes. Fig.8b shows the density distribution of the computed results at $t = 0.25$. Compared with the results of the calculation on rectangular mesh(480*120 cells, Fig.8a), the computation without adaptation gives a similar result. The number of nodes used is about one third of the number of nodes in the rectangular mesh. Fig.8b,c show the density comparison between the uniform mesh and the adapted mesh. The adapted mesh is a result of two level adaptation on the uniform mesh. Again, the resolution of shock waves is greatly improved. The resolution of the contact discontinuity merits particular attention. Fig.9 - Fig.12 show local views of mesh, density and entropy distribution around the triple point. Due to the increased resolution, we can see the local flow pattern in detail. Since the contact discontinuity is unstable, the wavy motion originated from the triple point is growing, leading to a non-similar Kelvin-Helmholtz rollup along the principle slip line. The normal shock reflected from the solid wall are slightly curved due to the shock-vortex interaction. LED-Csplitted and LED-BGK schemes yield extremely good results while LED-CUSP scheme is slightly diffusive. Similar numerical results on the instability of the contact discontinuity have been reported by Berger and Colella. These results are based on a PPM solver combined with AMR(Automatic Mesh Refinement) technique on rectangular mesh([6]).

Finally, we consider a moving shock interaction over a circular cylinder. A moving shock with the speed of $M_s = 2.81$ passes through the circular cylinder, which induces shock-shock, shock-contact discontinuity interactions and high expansions terminated by weak shocks. Fig.13 shows mesh and density distribution at $t = 0.55$. The adapted mesh is slightly asymmetric with respect to the center line because of the asymmetry of the initial mesh. All LED schemes present detail flow pattern with a

slight difference in resolving the contact discontinuity.

5 Conclusions

Within the finite volume framework, an accurate and robust LED-BGK solver has been developed on unstructured adaptive mesh. In the initial reconstruction step, the LED interpolation has been implemented to obtain left and right values across the cell interface. In the gas evolution step, the integral solution of the collisional BGK model is used to compute the numerical fluxes. It has been observed that the BGK model provides a good alternative to Riemann solvers for the gas evolution step. Numerical results indicate that the LED-BGK solver captures both physical discontinuities and expansion regions very well without spurious oscillations. Numerical comparison with the characteristic splitting and CUSP splitting also confirms the accuracy and robustness of the current BGK solver. The h -refinement mesh adaptation method greatly improves the resolution of physical discontinuities and shows the details of local flow patterns. This validates the capability of the current numerical approach to provide a highly accurate solution on complex geometry.

Acknowledgement

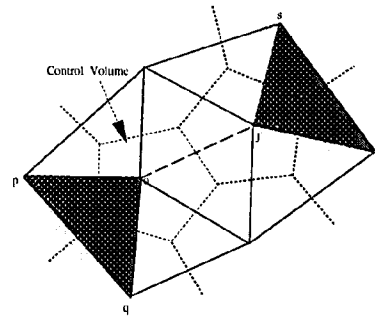
This research is supported by Grant URI/AFOSR F49620-93-1-0427 for all authors. The authors thank Dr. T.J. Baker for valuable advices on mesh generation and adaptation.

References

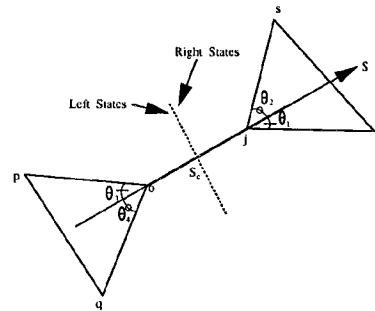
- [1] Arminjon, P. and Dervieux, A., "Construction of TVD-like artificial viscosities on 2-dimensional arbitrary FEM grids," INRIA Report 1111, 1989
- [2] Baker, T.J., "Triangulations, Mesh Generation and Point Placement Strategies," Proceedings Frontiers of Computational Fluid Dynamics, edited by Caughey pp. 101-115, Cornell University, Ithaca, New York, 1994.
- [3] Baker, T.J., "Mesh Adaptation Strategies for Problems in Fluid Dynamics," To appear in Finite Elements in Analysis and Design, 1996.
- [4] Baum, P.P. and Löhner, R., "Numerical Simulation of Shock Interaction with a Modern Main Battlefield Tank," AIAA 22nd Fluid Dynamics Conference, AIAA paper 91-1666, 1991.

- [5] Berger, M.J. and Jameson, A., "Automatic Adaptive Grid Refinement for the Euler Equations," *AIAA J.*, Vol. 23, pp. 561-568, 1985.
- [6] Berger, M.J. and Colella, P., "Local Adaptive Mesh Refinement for Shock Hydrodynamics," *J. Comp. Phys.*, Vol. 82, pp. 64-84, 1989.
- [7] Delanyne, M. and Essers, J.A., "An Accurate Finite Volume Scheme for Euler and Navier-Stokes Equations on Unstructured Adaptive Grids," *Proc. 12th AIAA CFD Conference*, AIAA paper, 95-1710-CP, 1995
- [8] Einfeldt, B. Munz, C.D, Roe, P.L. and Sjögreen, B., "On the Godunov-type Methods near Low Density," *J. Comp. Phys.*, Vol. 92, pp. 273, 1991.
- [9] Godunov, S.K., "A Difference Scheme for the Numerical Computation of Discontinuous Solutions of Hydrodynamic Equations," *Math. Sbornik*, Vol. 47, pp. 271, 1959.
- [10] Harten, A., "High Resolution Schemes for Hyperbolic Conservation Laws," *J. Comp. Phys.*, Vol. 49, pp. 357, 1983.
- [11] Harten, A. Enquist, B. Osher, S. and Chakravarthy, S., "Uniformly Higher- Order Accurate Essentially Non-Oscillatory Schemes III," *J. Comp. Phys.*, Vol. 171, pp. 231, 1987.
- [12] Harten, A. Lax, P.D. and Van Leer, B., "On the Upstream Differencing and Godunov-type Schemes for Hyperbolic Conservation Laws," *SIAM Rev.*, Vol. 25, pp. 35, 1983.
- [13] Jameson, A., "Positive Schemes and Shock Modelling for Compressible Flows," *Int. J. Num. Met. Flu.*, Vol. 20, pp. 743-776.
- [14] Johnson, C. and Hansboro, P., "Adaptive Finite Element Methods in Computational Mechanics," *Comp. Meth. Appl. Mech. and Eng.*, Vol. 101, pp. 143-181, 1992.
- [15] Kim, C.A. and Jameson, A., "Flux Limited Dissipation Schemes for High Speed Unsteady Flows," *12th AIAA CFD Conference*, AIAA paper 95-1738-CP, 1995.
- [16] Kim, C.A. Xu, K. Martinelli, L. and Jameson, A., "Analysis and Implementation of the Gas-Kinetic BGK Scheme for Computational Gas Dynamics," Accepted for Publication in *Int. J. Num. Meth. Flu.*, 1996.
- [17] Kogan, M.N., *Rarefied Gas Dynamics*, Plenum Press, New York.
- [18] Löhner, R., "An Adaptive Finite Element Scheme for Transient Problems in CFD," *Comp. Meth. App. Mech. and Eng.*, Vol. 61, pp.323-338, 1987.
- [19] Löhner, R. Morgan, K. Peraire, J. and Vahdati, M., "Finite Element Flux-Corrected Transport(FEM-FCT) for the Euler and Navier-Stokes Equations," *Int. J. Num. Met. Flu.*, Vol. 7, pp. 1093-1109, 1987.
- [20] Macrossan, M.N. and Oliver, R.I., "A Kinetic Theory Solution Method for Navier-Stokes Equations," *Int. J. Num. Met. Flu.*, Vol. 17, pp. 177, 1993.
- [21] Mandal, J.C. and Deshpande, S.M., "Kinetic Flux Vector Splitting for Euler Equations," *Computers and Fluids*, Vol. 23, pp. 447, 1994.
- [22] Mitty, T.J. Baker, T.J and Jameson, A., "Solution of Three-Dimensional Supersonic Flowfields via Adapting Unstructured Meshes," *Computers and Fluids*, Vol. 22, pp. 271-283, 1993.
- [23] Perthame, B., "Second-Order Boltzmann Schemes for Compressible Euler equation in One and Two Space Dimensions," *SIAM J. Num. Anal.*, Vol. 29, No. 1, 1992.
- [24] Quirk, J., "A Contribution to the Great Riemann Solver Debate," *Int. J. Num. Met. Flu.*, Vol. 18, No. 6, 1994.
- [25] Rausch, R.D. Batina, J.T. and Yang, H.T.Y., "Spatial Adaptation Procedures on Tetrahedral Meshes for Unsteady Aerodynamic Flow Calculations," *31st Aerospace Sciences Meeting and Exhibit*, AIAA paper 93-0670, Reno, 1993.
- [26] Rebay, S., "Efficient Unstructured Mesh Generation by Means of Delaunay Triangulation and Bowyer-Watson Algorithm," *J. Comp. Phys.*, Vol. 106, pp. 125-138, 1993.
- [27] Roe, P.L., "Approximate Riemann Solvers, Parameter Vectors and Difference Schemes," *J. Comp. Phys.*, Vol. 43, pp. 357, 1981.
- [28] Shu, C.W. and Osher, S., "Efficient Implementation of Essentially Non-Oscillatory Shock-Capturing Schemes II," *J. Comp. Phys.*, Vol.82, pp. 32, 1989.
- [29] Tatsumi, S. Martinelli, L. and Jameson, A., "Design, Implementation and Validation of Flux Limited Dissipation Schemes for the Compressible Navier-Stokes Equations," *AIAA J.*, Vol. 33, pp. 252, 1995.

- [30] Weatherhill, N.P. Hassan, O. Marchant, M.J. and Marcum, D.L., "Adaptive Inviscid Flow Solutions for Aerospace Geometries on Efficiently Generated Unstructured Tetrahedral Meshes," Proc. 11th AIAA CFD Conference, AIAA paper 93-3390-CP, 1993.
- [31] Woodward, P. and Colella, P., "The Numerical Simulation of Two-dimensional Fluid Flow with Strong Shocks," J. Comp. Phys., Vol. 54, pp. 115, 1984.
- [32] Xu, K. and Predergast, K.H., "Numerical Navier-Stokes Solutions from Gas-Kinetic Theory," J. Comp. Phys., Vol. 114, pp. 9, 1994.
- [33] Xu, K. Martinelli, L. and Jameson, A., "Gas-Kinetic Finite Volume Methods, Flux-Vector Splitting and Artificial Diffusion," J. Comp. Phys., Vol. 120, pp. 48-65, 1995.
- [34] Xu, K. Kim, C.A. Martinelli, L. and Jameson, A., "BGK-Based Schemes for the Simulation of Compressible Flow," Int. J. Comp. Flu. Dyna., Vol.7, pp. 213-235, 1996



1a: Control Volume, Edge(l_{jo}) and Adjacent Triangles



1b: Local Coordinates(S)

Figure 1: Interpolation on Unstructured Mesh

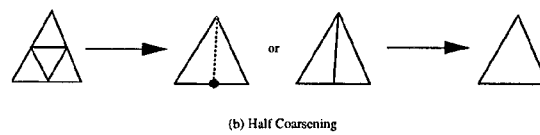
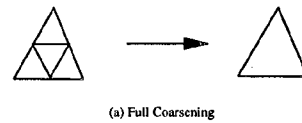
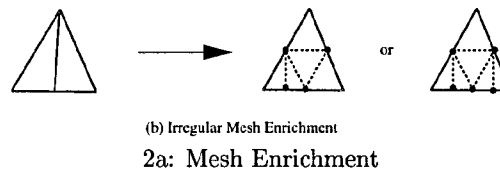
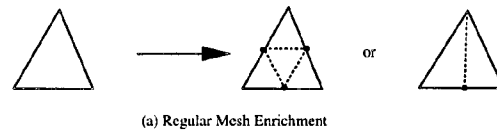
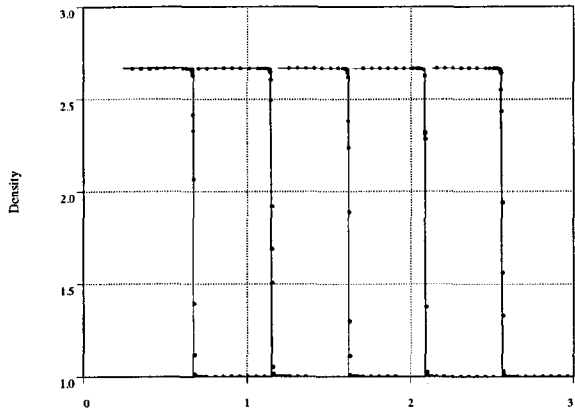
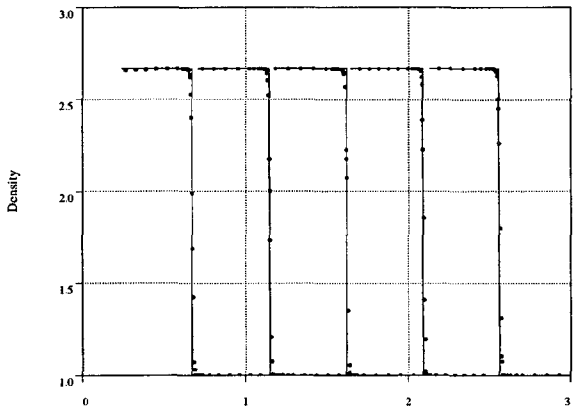


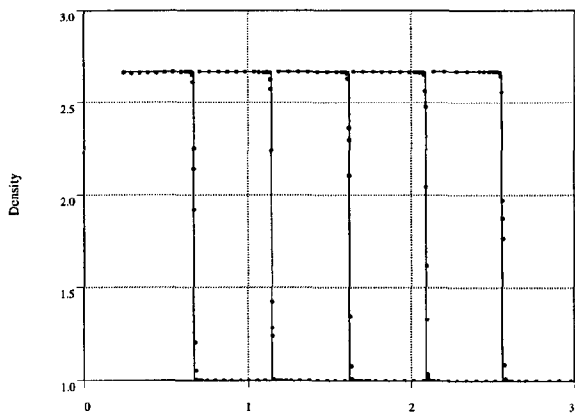
Figure 2: Mesh Adaptation Steps



3a: Density Profile with LED-Csplint Scheme at $t = 0.2, 0.4, 0.6, 0.8, 1.0$

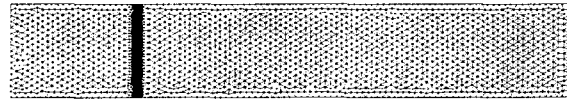


3b: Density Profile with LED-CUSP Scheme

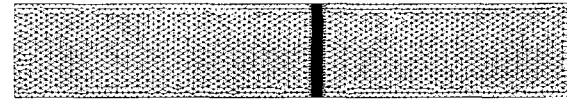


3c: Density Profile with LED-BGK Scheme

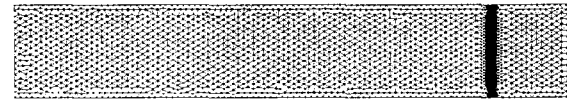
Figure 3: Two-Dimensional Moving Shock with $M_s = 1.5$. Computed Results($\cdot\cdot$) are Compared with Exact Solutions($-$)



4a: $t = 0.2$. 3503 Nodes



4b: $t = 0.6$. 3474 Nodes



4c: $t = 1.0$. 3534 Nodes

Figure 4: Adapted Mesh Distribution

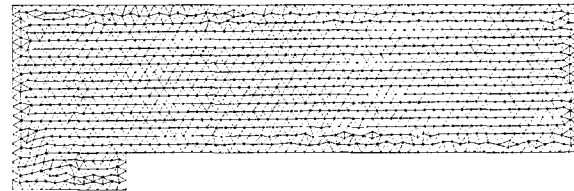
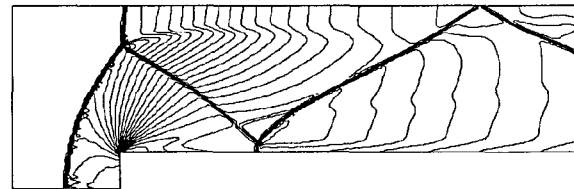
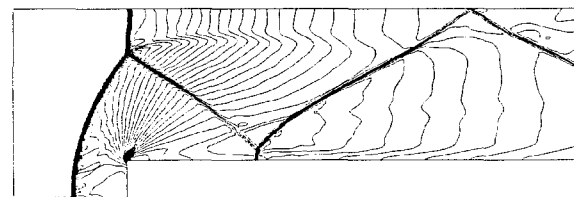


Figure 5: Typical Mesh Distribution

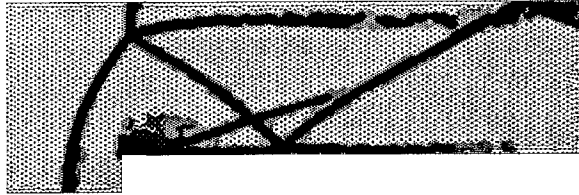


6a: Structured Meshes (16140 Cells)

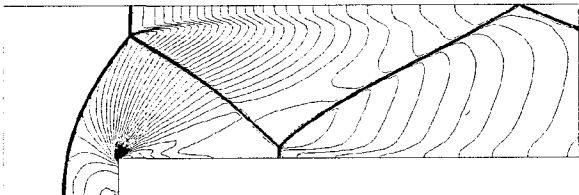


6b: Unstructured Meshes (18110 Nodes)

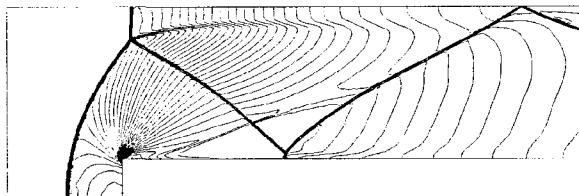
Figure 6: Density Distribution with LED-BGK Scheme at $t = 4.0$



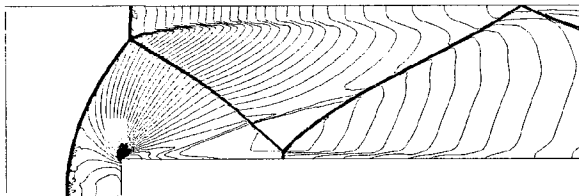
7a: Typical Adapted Mesh Distribution



7b: Density Contours with LED-Csplit Scheme

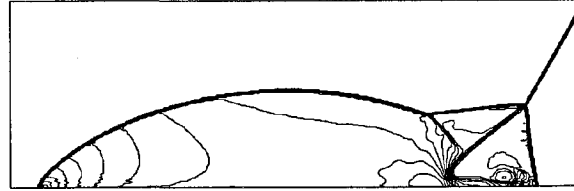


7c: Density Contours with LED-CUSP Scheme

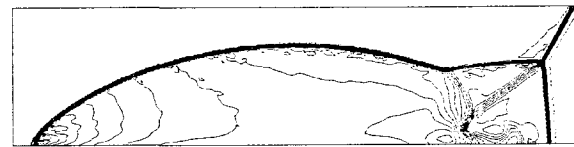


7d: Density Contours with LED-BGK Scheme

Figure 7: Forward Facing Step. LED Schemes at $t = 3.0$



8a: Structured Mesh (480 x 120 Cells)



8b: Unstructured Mesh (17000 Nodes)



8c: Unstructured Adapted Mesh (36245 Nodes)

Figure 8: Double Mach Reflection. LED-BGK Scheme

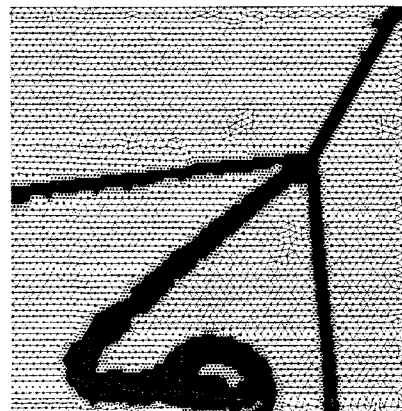
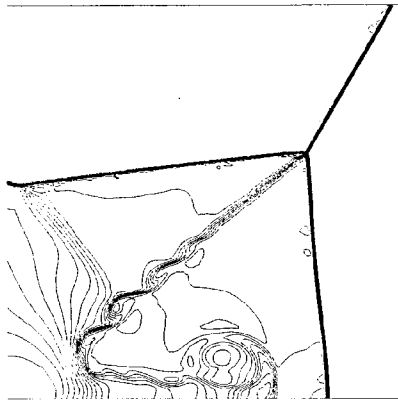
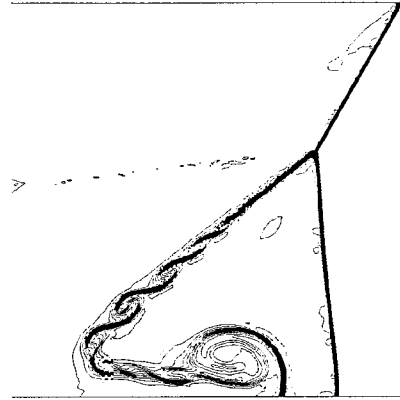


Figure 9: Double Mach Reflection. Typical Adapted Mesh Distribution

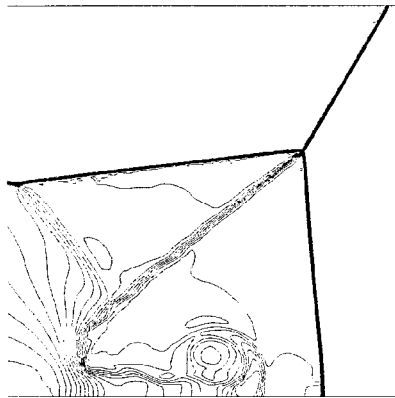


10a: Density Contours

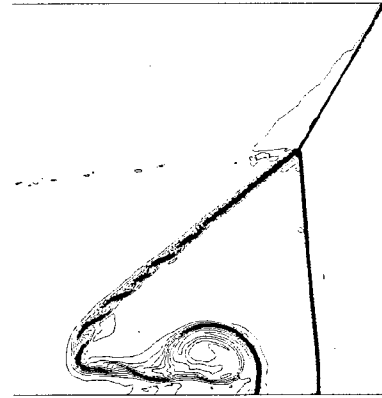


10b: Entropy Contours

Figure 10: Local View of Double Mach Reflection. LED-Csplit Scheme

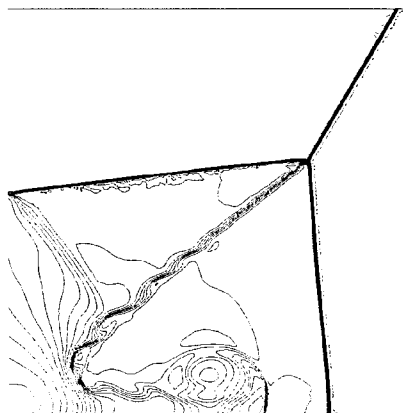


11a: Density Contours

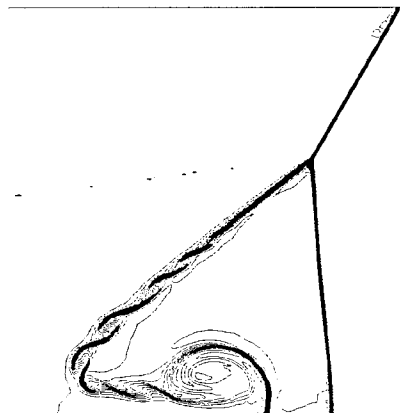


11b: Entropy Contours

Figure 11: Local View of Double Mach Reflection. LED-CUSP Scheme

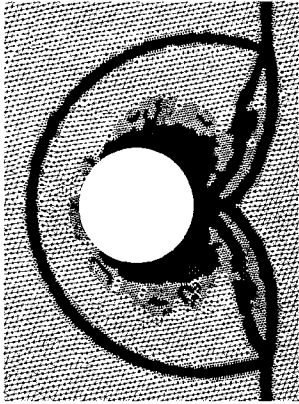


12a: Density Contours

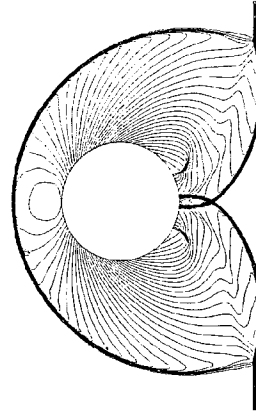


12b: Entropy Contours

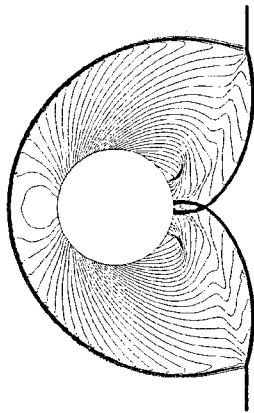
Figure 12: Local View of Double Mach Reflection. LED-BGK Scheme



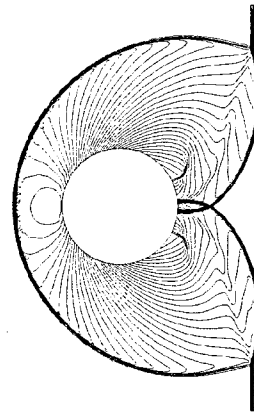
13a: Typical Adapted Mesh



13b: LED-Csplitted Scheme



13c: LED-CUSP Scheme



13d: LED-BGK Scheme

Figure 13: Moving Shock over a Cylinder. Density Contours